ADVANCED MATERIALS TECHNOLOGIES
www.advmattechnol.de

A Microvascular-Based Multifunctional and Reconfigurable Metamaterial

*Urmi Devi, Reza Pejman, Zachary J. Phillips, Pengfei Zhang, Soheil Soghrati, Kalyana B. Nakshatrala, Ahmad R. Najafi, Kurt R. Schab, and Jason F. Patrick**

Nearly all-natural and synthetic composites derive their characteristic attributes from a hierarchical makeup. Engineered metamaterials exhibit properties not existing in natural composites by precise patterning, often periodically on size scales smaller than the wavelength of the phenomenon they influence. Lightweight fiber-reinforced polymer composites, comprising stiff/strong fibers embedded within a continuous matrix, offer a superior structural platform for micro-architectured metamaterials. The emergence of microvascular fiber-composites, originally conceived for bioinspired self-healing via microchannels filled with functional fluids, provides a unique pathway for dynamic reconfigurable behavior. Demonstrated here is the new ability to modulate both electromagnetic and thermal responses within a single structural composite by fluid substitution within a serpentine vasculature. Liquid metal infiltration of varying density micro-channels alters polarized radiofrequency wave reflection, while water circulation through the same vasculature enables active-cooling. This latest approach to control bulk property plurality by widespread vascularization exhibits minimal impact on structural performance. Detailed experimental/computational studies, presented in this paper, unravel the effects of micro-vascular topology on macro-mechanical behavior. The results, spanning multiple physics, provide a new benchmark for future design optimization and real-world application of multifunctional and adaptive microvascular composite metamaterials.

1. Introduction

The survival of living organisms hinges on a multitude of homeostatic and metabolic functions including temperature regulation, nutrient delivery, waste removal, damage repair, and regeneration.[1] These functionalities are largely enabled by fluid transport via internal vasculatures.[2,3] Mimicking microvasculature in synthetic materials has proven to be a viable route for achieving bio-inspired, multi-functionality such as self-healing,[4–9] active-cooling,[10–14] electromagnetic reconfiguration,[15–19] and structural health monitoring.[20–23]

Early approaches for creating vasculature relied on embedding permanent hollow elements,[24–26] removal of temporary cores,[27–29] or micro-machining;[30–32] however, such approaches can only produce straight (i.e., 1D), segregated microchannels. More complex 2D and 3D interconnected vascular networks can be fabricated using stochastic processes such as electric discharge[33] or controlled deposition of sacrificial materials, for example, direct ink writing.[34–36] However, it remains challenging to create interconnected, multi-dimensional, and multi-scale vasculature in fiber-reinforced composites due to the heterogeneous material makeup and harsh processing conditions (e.g., elevated temperatures and compaction pressures).[37,38] The vaporization of sacrificial components (VaSC),[39] a recent technique based on thermal depolymerization of sacrificial poly(lactic) acid (PLA), overcomes such processing limitations and enables the fabrication of intricate and interconnected microvascular networks in structural composites. Latest additive manufacturing implementations for sacrificial PLA,[40,41] namely fused-deposition modeling, have furthered the fabrication envelope enabling greater flexibility in vascular composite design.

U. Devi, Z. J. Phillips, J. F. Patrick
Department of Civil, Construction, and Environmental Engineering
North Carolina State University
Raleigh, NC 27695, USA
E-mail: jfpatric@ncsu.edu

R. Pejman, A. R. Najafi
Department of Mechanical Engineering and Mechanics
Drexel University
Philadelphia, PA 19104, USA

The ORCID identification number(s) for the author(s) of this article can be found under https://doi.org/10.1002/admt.202100433.

P. Zhang, S. Soghrati
Department of Mechanical and Aerospace Engineering
The Ohio State University
Columbus, OH 43210, USA

K. B. Nakshatrala
Department of Civil and Environmental Engineering
University of Houston
Houston, TX 77204, USA

K. R. Schab
Department of Electrical and Computer Engineering
Santa Clara University
Santa Clara, CA 95053, USA

DOI: 10.1002/admt.202100433

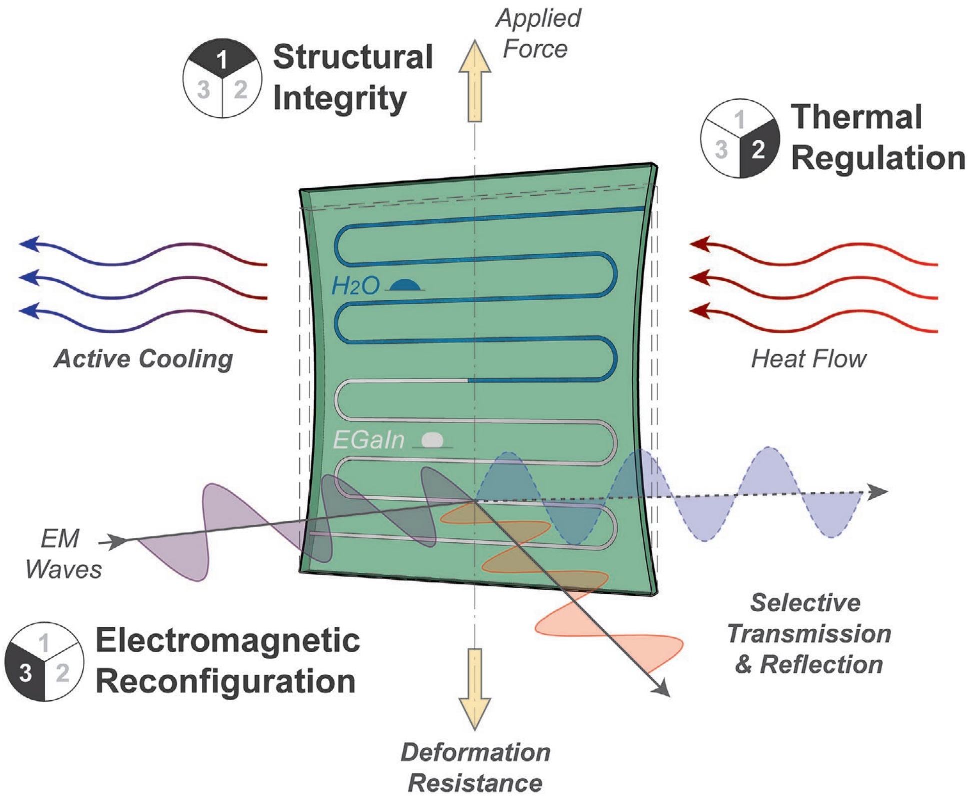

Figure 1. Multifunctional microvascular composite concept. Swapping different fluids within a pervasive serpentine vasculature enables multi-physics tuning of electromagnetic (via eutectic gallium–indium, EGaIn, liquid-metal) and thermal (via distilled water, H_2O) properties within a structural, fiber-reinforced composite.

The ability to incorporate dynamic, multi-functionality in vascular fiber-composites stems from the physical and chemical properties of the fluid sequestered within the vasculature. Examples include conductive liquid metals for electromagnetic modulation,[42,43] coolants for thermal management,[44,45] and reactive agents for self-healing.[46,47] Such prior studies have demonstrated how to achieve various functionalities, independently, in different composite platforms. In this paper, we modulate and characterize electromagnetic (EM) and thermal properties within the same structural composite while retaining its mechanical performance. **Figure 1** provides a general overview of our approach to microvascular multi-functionality within a structural glass fiber/epoxy matrix composite. Electromagnetic reconfiguration (i.e., frequency modulation and filtering) is achieved through infusion and withdrawal of eutectic gallium–indium (EGaIn) liquid metal[48] whereas thermal regulation (i.e., active-cooling) is achieved by circulation of water through the internal vasculature.

Our multi-functional material system can be considered a (reconfigurable) metamaterial since the dynamic properties are achieved via the physical placement of base materials (e.g., hollow vasculature, functional fluids, epoxy matrix, reinforcing fibers). Classically, a metamaterial is an engineered composite to realize desired functionalities that are not otherwise attainable with base materials; these macroscopic properties are derived from physical placement of constituents rather than chemical composition.[49–51] The realization of a metamaterial has created opportunities in various emerging fields such as phononics,[52] photonics,[53,54] mechanical topological insulators,[55,56] and programmable materials.[57,58] Through intelligent material architecting, researchers have been able to: achieve unique mechanical (e.g., negative/zero Poisson's ratio[59–63]), optical (e.g., negative refractive index,[64] optical cloaking[65]), and electromagnetic (e.g., negative permittivity,[66] EM cloaking[67]) properties; tune wave propagation characteristics (e.g., tailored bandgaps,[68–70] defect-immune wave motion,[71] seismic wave barriers, and foundations[72–74]); attain bulk/topological thermal systems;[75,76] and build reconfigurable/flexible mechanical systems.[77,78] However, prior research has focused on metamaterials with a single functionality. Motivated by these pioneering works, we take a modest step toward achieving a multitude of functionalities in a single structural composite.

To realize such a composite, we 3D printed sacrificial templates to create inverse-replica serpentine micro-channels (see Figure 1) via the VaSC process. This vascular topology is selected for its demonstrated versatility in functionality,[79–82] geometric regularity for manufacturing consistency, and presence of a single flow path for simplicity of the fluidic system. We selected a fixed channel diameter of ≈ 500 µm based on several factors: i) sacrificial PLA is easily extruded through a standard 0.5 mm 3D printer nozzle; ii) to alleviate structural impact based upon a prior study (in a different composite system) that has shown in-plane mechanical properties degrade appreciably beyond 500 µm diameter;[83] and iii) to minimize pressure drop which scales inversely proportional to the 4th power of the channel diameter based upon the Hagen–Poiseuille relation[84] (i.e., a 250 µm diameter channel has 16 times the pressure drop of a 500 µm channel). Leveraging analytical modeling, we designed and constructed a suitable vascular density (spacing, s = 2, 4, 6, and 8 mm) for liquid metal-based polarization-specific electromagnetic shielding. Experiments were conducted to validate the EM shielding efficacy along with water-based active-cooling and structural performance. While a particular spacing for each function results in enhanced performance, the same spacing does not necessarily translate to optimal outcomes for other attributes. Thus, it is crucial to understand competing effects and target application requirements in order to tailor the microvascular system for optimum overall performance. Here we employed computational analyses to better understand the effects of widespread vascularization on structural integrity (via finite element discretization of quasi-static equilibrium equations) and heat transfer (via finite volume discretization of momentum–energy equations).

An outline for the rest of this article is as follows. Section 2 describes the experimental methods. Section 3 details the electromagnetic reconfiguration study. Section 4 shows that our vascularization approach does not adversely compromise structural integrity and provides a deeper insight into mechanical performance. Next, in Section 5 we examine thermal regulation and quantify cooling efficiency of our multifunctional metamaterial. Finally, the main research findings are summarized along with a discussion on potential future research endeavors in Section 6.

2. Experimental Section

2.1. Microvascular Composite Fabrication

Microvasculature of circular cross-section (515 µm diameter) and varying channel spacings (s = 2, 4, 6, and 8 mm) was created in glass-fiber/epoxy-matrix composites by: i) 3D printing sacrificial PLA templates;[40] ii) vacuum-assisted resin transfer molding (VARTM) of the reinforcing preform containing the templates; iii) VaSC process[39] to remove the templates from solidified composites. A commercially available 3D printer (Lulzbot TAZ 6) was employed to create the single print layer sacrificial templates via fused deposition modeling with a nozzle temperature 185 °C onto a heated bed at 65 °C; before removing the printed templates, the bed temperature was naturally cooled to 40 °C (below the glass-transition temperature of PLA ≈ 57 °C[40]) to limit distortion. Six plies of an eight-harness (8H) satin weave E-glass fabric (Style 7781, Fibre Glast Developments Corp.) were stacked in a $[90/0]_3$ layup sequence with 3D printed templates that were solvent-bonded to reinforcing plies using acetone and symmetrically placed between.

The single-layer electromagnetic and thermal composites contained one printed serpentine template placed at the mid-plane (i.e., between plies 3/4) of the 6-layer stack while dual-layer composites contained two printed templates placed symmetrically between layers 2/3 and 4/5. The single-layer tension samples contained one printed template of parallel lines placed at the mid-plane of the 6-layer stack with the longitudinal samples aligned to the 0° plies while the transverse samples were aligned with the 90° plies. For all samples, the printed templates were spatially arranged across the composite preform to balance the sacrificial inclusions and minimize panel warping during composite fabrication.

Epoxy-resin (Araldite LY/Aradur 8605, 100:35 by wt, Huntsman Advanced Materials LLC) was infused into the composite preform using the VARTM process at 2 Torr (abs.) vacuum until complete fabric wetting and then reduced to 380 Torr (abs.) vacuum until resin solidification. Vacuum was released after 24 h at room temperature and the glass-fiber composite was post-cured in a forced convection oven for 2 h at 121 °C followed by 2 h at 150 °C. The average thickness of single-layer vascular composites increased as the spacing of sacrificial serpentine templates decreased; for a fixed (s = 6 mm) spacing, the dual-layer samples were thicker than the single-layer counterparts (see **Table 1**). When possible, composite samples for a particular study were fabricated from the same panel to minimize the effect of possible fiber volume fraction and ply orientation variations.

Composite samples were then cut to desired areal dimensions (Table 1) exposing vascule cross-sections using a diamond-blade wet-saw. Compressed air-dried composite samples underwent the VaSC process in a vacuum oven at 200 °C under ≈ 10 Torr (abs.) of vacuum for 12 h. Vaporization of embedded sacrificial templates resulted in inverse replica circular-shaped microchannels with a diameter of 515 ± 20 µm.

2.2. Liquid Metal Preparation

EGaIn (75.5 wt% Ga, 24.5 wt% In) was prepared by melting gallium in a container placed within a water bath on a hot plate heated to 80 °C, to which indium pellets were added and remained at temperature until alloyed. The liquid-metal was then cooled to room temperature and immediately stored in 1 mL syringes to mitigate oxide formation.

2.3. Tension Testing

To prevent sample crushing in the load-frame grips, 50 mm long fiberglass tabs (Garolite G-10/FR4) with a 10° taper were cut to the same width as samples and bonded to each face with

Table 1. Vascular composite sample dimensions.

Sample type	Length × Width	Average thickness			
		s = 2 mm	s = 4 mm	s = 6 mm	s = 8 mm
Electrical	100 × 100 mm				
Structural	Longitudinal: 20-22 × 200 mm Transverse: 17 × 200 mm	1.8 mm	1.75 mm	Single-layer: 1.65 mm Dual-layer: 1.75 mm	1.5 mm
Thermal	100 × 100 mm				

a high shear strength adhesive (3M Scotch-Weld DP460NS). The adhesive was cured at RT for 8 h to reach full-strength. To prepare the tension samples for DIC, the front/back and side profiles were spray-painted matte white followed by speckling with matte black paint to produce a high-contrast speckle pattern (Supporting Information). To obtain higher-resolution strain measurements around micro-channels in the transverse samples, a finer black speckle pattern was applied using an airbrush (Iwata HP-BCS ECL2000).

Samples were aligned/clamped in mechanical wedge grips and tested at a rate of 1.5 mm min^{-1} while force and crosshead displacement were captured by a computer running MTS TestSuite TW Elite software. The slower test rate than the ASTM D3039[85] standard recommends (≈ 2.0 mm min^{-1}) was specified to increase the number of DIC images captured at 2 Hz during testing. Two cameras were used to capture the full-field displacements of the front and back faces while an additional camera used to capture side profile measurements. Time-stamped images were subsequently analyzed using VIC-2D software (Correlated Solutions) to calculate strain. Strain and load data were then correlated by matching time of failure.

2.4. Thermal Evaluation

To provide more uniform heat distribution, a copper plate (100 × 100 × 6 mm) was adhered to the bottom of the vascular composites via thermal grease and placed atop the resistive heater (Omega, part # KH608/2). The side profiles of the composite, copper plate, and heater assembly were insulated by 5 mm thick chloroprene rubber foam. The bottom of the entire assembly was also insulated by two 12.7 mm thick pieces of balsa wood. The composite top surface was free to convect and radiate heat to the surroundings, and we recorded the surface temperature by an overhead-mounted infrared (IR) camera (FLIR, model # A655sc). Distilled water was distributed through the vascular samples via tubing connected to a peristaltic pump (Cole-Parmer Masterflex, item # EW-07522-30) and cylindrical micro-nozzles inserted into the inlet/outlet, which were oversized by machining to 810 µm diameter to reduce pressure drop and provide a tight fit for the 21 gauge nozzles (McMaster-Carr, part # 75165A679). For the dual-channel configuration, channels adjacent to the inlet/outlet orifices were shortened by ≈2 mm to prevent penetration of adjacent, machined nozzle entries (Supporting Information). To measure the coolant temperature, two K-type thermocouples (Phidgets, part # TMP4103_0) were inserted into the center of the tubing at the connection junction of the inlet and outlet nozzles. The ambient temperature was also recorded by an additional thermocouple placed at the same height as the IR camera to provide measurement redundancy and ensure accuracy of the readings.

3. Electromagnetic Reconfiguration

Reconfigurable electronics have emerged to provide bandwidth versatility in an increasingly occupied and monitored radio frequency (RF) spectrum. While various approaches rely on surface-mounted devices or structural changes (e.g., origami) to modulate electromagnetic signature,[86,87] structurally-embedded electronics offer enhanced physical protection and reduce overall material footprint. Liquid metal microfluidics is an emerging embedded modality for implementing electromagnetic (EM) reconfiguration in a variety of material systems.[15,17,43,88–90] This internal strategy provides EM flexibility without external geometrical modifications, especially important for aerodynamic structures, and eliminates additional bias circuitry.[86] While several prior studies in structural composites demonstrate promise for local topology changes using liquid metal,[15,17,19] the ability of pervasive liquid metal patterning to achieve reconfiguration of equivalent bulk material properties—a main focus of this section—has been studied to a much lesser extent.

Applying our multipurpose serpentine vasculature as an integrated platform for widespread electromagnetic reconfiguration, we utilized EGaIn[91] within microchannels for reconfigurable, polarization selective reflection of electromagnetic waves. In our experimental system, (**Figure 2**a), we placed the reconfigurable composite screen (≈ 100 mm square) behind an omnidirectional, vertically oriented transmitting monopole antenna at varying distances (25 mm < d < 40 mm). The antenna is self-resonant at 5 GHz and the entire system is placed over a 250 mm square copper ground plane. We located a copolarized broadband receiving horn in the far-field (≈ 1 m) of the transmitting antenna in the broadside direction with respect to the screen location, see Figure 2a. In this configuration, the forward transmission $|S_{21}|$ between transmitter and receiver consists of direct and reflected components, and the latter component is dependent on the reflective state of the composite screen.

To assess the efficacy of the screen's reconfigurable polarization-specific reflectivity state, we measured forward transmission between the antenna and the receiving horn over a bandwidth of 3 to 7 GHz. We normalized the transmission data at each frequency point using a control data set $|S_{21}^0|$ acquired with no screen present. Note that this normalization process removes the effects of antenna impedance mismatch as measured within the control measurement. Assuming plane wave behavior and neglecting minor antenna impedance changes introduced by the screen, an analytic homogenized model[92,93] for the measurement is given by:

$$\frac{|S_{21}|}{|S_{21}^0|} = |1 + \mathrm{e}^{-\mathrm{j}2kd}\Gamma| \tag{1}$$

where k is the free space wave number in the incident field and Γ is the reflection coefficient of the homogenized screen, available analytically for both single- and dual-channel screens[92] (Section S1, Supporting Information). Based on the analytical model assumptions, the reflector screen should be large enough to be considered infinite and the serpentine microchannel spacing (s) should be small with respect to wavelength (λ), that is, $s \ll \lambda$ (≈ 4.3 cm at 7 GHz), for the screen to act as polarization selective surface when filled with EGaIn.

Two sets of experiments were carried out using single- and dual-channel screens (Figure 2b). Single-channel screens had channel orientations ($\hat{\mathbf{c}}$) aligned or copolarized with the electric field ($\hat{\mathbf{e}}$) radiated by the transmitting monopole (i.e., $\hat{\mathbf{e}} \cdot \hat{\mathbf{c}}_{\parallel} = 1$). In addition to this copolarized channel, the

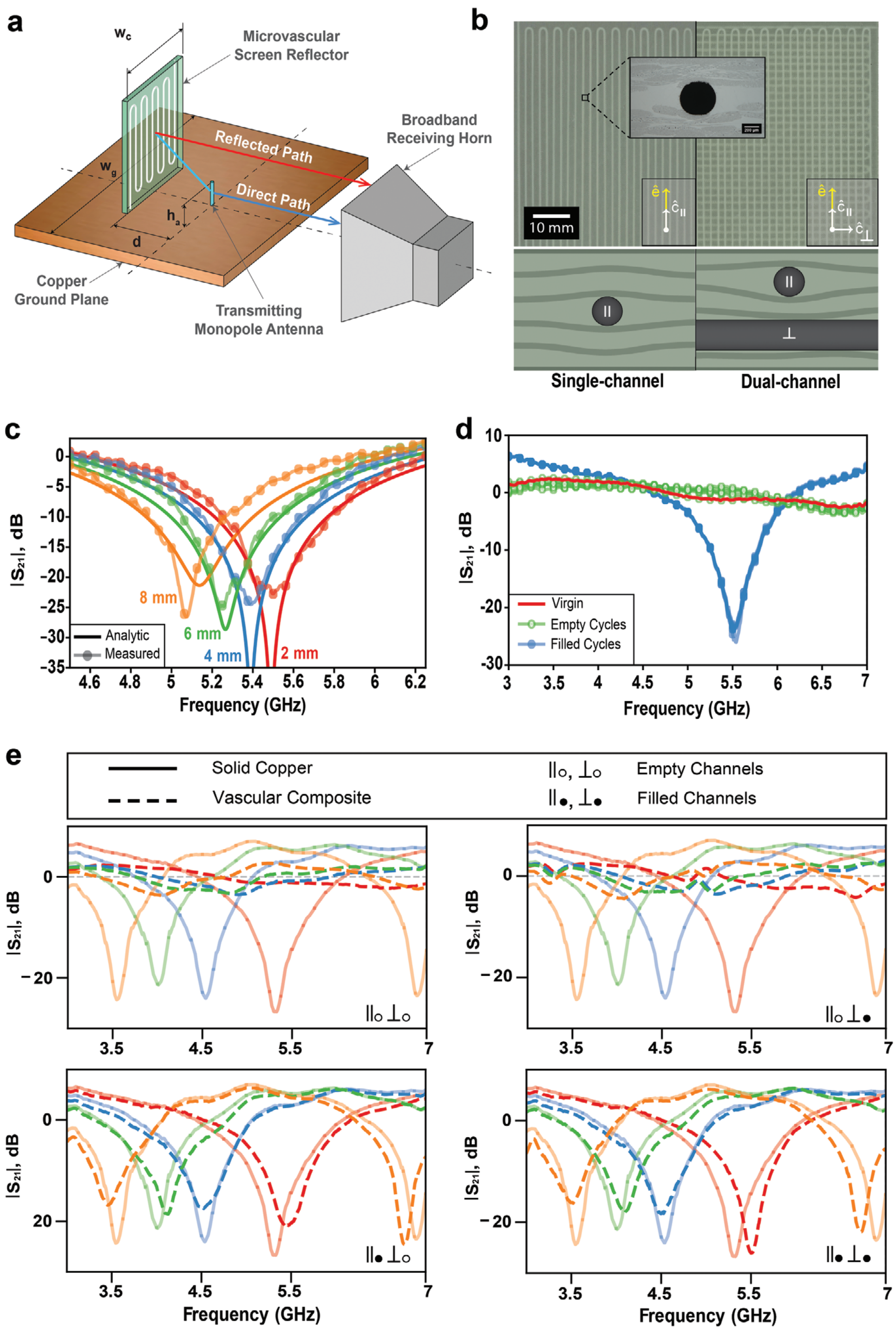

Figure 2. Electromagnetic reconfiguration. a) Schematic of experimental setup for measuring forward transmission ($|S_{21}|$) between a monopole antenna and broadband receiving horn with the vascular reflector screen located behind the antenna. Dimensions used in experiments: $h_a = 15$ mm, $w_c = 100$ mm, $w_g = 250$ mm, $d \in [25, 40]$ mm. b) (Top) Single-channel (left) and dual-channel (right) composites containing 3D printed sacrificial serpentine templates with optical micrograph inset revealing post-VaSC microchannel (scale bar = 500 µm); (Bottom) Schematics depicting interlaminar location of microchannels in single- and dual-channel configurations. c) Forward transmission for single-channel configurations comparing the analytic model and experimental measurement with panel offset distance $d = 27.5$ mm. d) Virgin $|S_{21}|$ along with six repeat fill and empty cycles for the single-channel screen with 2 mm spacing. Shaded empty/filled regions depict data envelope for all repeat measurements at each frequency point. e) Forward transmission for dual-channel screens under four possible configurations (i.e., polarization states) compared to a solid copper panel.

dual-channel screens contained a channel orthogonal to the field polarization, $(\hat{\mathbf{e}}\cdot\hat{\mathbf{c}}_\perp = 0)$. Each micro-channel can be independently emptied and/or filled with EGaIn that results in two ($\|_\circ$ and $\|_\bullet$) and four ($\|_\circ\perp_\circ$, $\|_\circ\perp_\bullet$, $\|_\bullet\perp_\circ$, and $\|_\bullet\perp_\bullet$) effective reflectivity states for single-channel and dual-channel configurations, respectively; where the subscripts $_\circ$ and $_\bullet$ denote empty and filled states of each channel.

Figure 2c illustrates the forward transmission results obtained for EGaIn filled single-channel screens with varying channel spacing. We observed a close agreement between experimental and analytical results for denser (i.e., s = 2, 4, and 6 mm) single-channel configurations, which reflects the validity of homogenized analytical model assumptions (i.e., $s \ll \lambda$). Prior studies have shown that repeated reconfiguration is challenging with EGaIn due to native oxide layer adhering to the interior channel wall that, without special treatment, leads to imperfect clearing of micro-channels.[94] To assess the impact here, we measured forward transmission for the single-channel screen with closest spacing (s = 2 mm) over six repeated cycles of filling and emptying with EGaIn. During each cycle, the channel was filled with EGaIn, measured using d = 27.5 mm in its filled state ($\|_\bullet$), flushed with ethanol, then measured again in its empty state ($\|_\circ$). We observed close agreement between each empty/fill cycle and the deviation from the virgin data set (taken before channels were first filled) was not cumulative (Figure 2d). Results in Figure 2d indicate that the presence of residual EGaIn has minimal impact on the screen performance, since our EM shielding system depends on bulk infiltration of liquid metal rather than precise, local delivery. Though depending on severity, local formation and possible accumulation of metal oxide could increase pressure drop by decreasing channel diameter and potentially alter heat transfer characteristics.

We also investigated the transmission behavior of the four polarization states for the dual-channel screen against that obtained using a solid copper panel (Figure 2e). Dual-channel screens behave as anisotropic conductive sheets only when co-polarized channels are filled ($\|_\bullet$) with EGaIn that results in reflection characteristics comparable to the copper control. Our polarization-selective metamaterial therefore provides flexibility in electromagentic (EM) performance via variable vascular topology and reconfigurability via liquid-metal transport.

We have shown that the vascularized structural composite infiltrated with EGaIn operates as a tunable, and reversible anisotropic EM reflective screen. We observed convergence between experimental and analytical evaluation with varying channel spacing. Better predictive performance for the reflective screens is achieved with higher vascular densities (s = 2, 4, and 6 mm) of the serpentine micro-channel. However, a denser vasculature results in an increased volume fraction of voids within the composite, which could negatively impact mechanical properties. Thus, it becomes crucial to understand the trade-off between vascular topology and structural integrity to fully leverage multiphysics performance in microvascular metamaterials.

4. Structural Integrity

While transport of functional fluids through pervasive vasculature shows promise in expanding the application space for fiber-reinforced polymer (FRP) composites, the enabling microvascular networks are, however, an intentional manufacturing defect to the hierarchical material layout. Embedding permanent hollow or solid sacrificial elements alters fiber-architecture, introducing fiber/ply waviness[21,83,95] and localized resin pockets[29,96,97] around vascular templates during fabrication by filling the displaced reinforcement with polymer matrix. An alternative approach to mitigate these microstructure alterations relies on small recesses cut into the continuous fiber reinforcement, which disrupts the load-bearing path and results in significant reductions to mechanical performance.[28] Regardless of the fabrication approach, internal micro-channels induce stress concentrations around the void. These vascularization artifacts produce different effects depending on the material system, vascular configuration, and loading conditions. We sought to unravel the impact of widespread serpentine vasculature on the tensile structural integrity of laminated woven composites; however, we acknowledge a more in-depth investigation focusing solely on mechanical properties is needed, which will be a part of our future studies.

Figure 3a highlights the effect of our variable density serpentine vasculature on laminated woven composite microstructure, where a closer spacing results in an increased volume fraction of epoxy resin pockets surrounding the vasculature. For the 2 and 4 mm spacings, a continuous midline resin-rich region is present, whereas discrete and channel-localized resin pockets are produced for the 6 and 8 mm spacings. Given that the epoxy matrix in this study has similar dielectric permittivity ($\varepsilon_r \approx 3$) to the glass-fiber reinforcement, there is minimal impact of these resin domains from an electromagnetic standpoint. However, since the mechanical properties (e.g., strength/modulus) of the fiber-composite and matrix are drastically different (shown in Figure 3b), a more pronounced effect on the structural integrity can be expected.

To investigate the mechanical impact of resin domains (which result from incorporation of sacrificial templates) and surface undulations (present even in plain, non-vascular composites due to woven reinforcement but augmented by sacrificial templating), we conducted a series of in-plane uniaxial tension tests according to ASTM D3039.[85] We evaluated the tensile behavior of neat epoxy dog-bones along with plain and vascular composites for all four spacings (s = 2, 4, 6, and 8 mm) with micro-channels in the longitudinal and transverse directions with respect to the loading axis as illustrated in Figure 3c,d. For each composite sample orientation, three samples of each type (plain/vascular) were fabricated from the same panel to minimize the effects of small, but unavoidable, variations in layered ply orientations and fiber volume fraction (Section S2, Supporting Information). Quasi-static, displacement-controlled experiments were conducted using an electro-mechanical load frame (MTS Exceed E45.105) equipped with a 100 kN load cell at a test rate of 1.5 mm min^{-1}. We employed 2D digital image correlation (DIC)[98,99] to accurately capture the full-field strain distributions of the front/back and side faces of the samples (see Experimental Section and Supporting Information).

Figure 3b shows representative stress versus (engineering) strain behavior under uniaxial tension for the neat epoxy and plain composite samples. The epoxy matrix, which is more compliant, exhibits nonlinear softening at higher strains while the

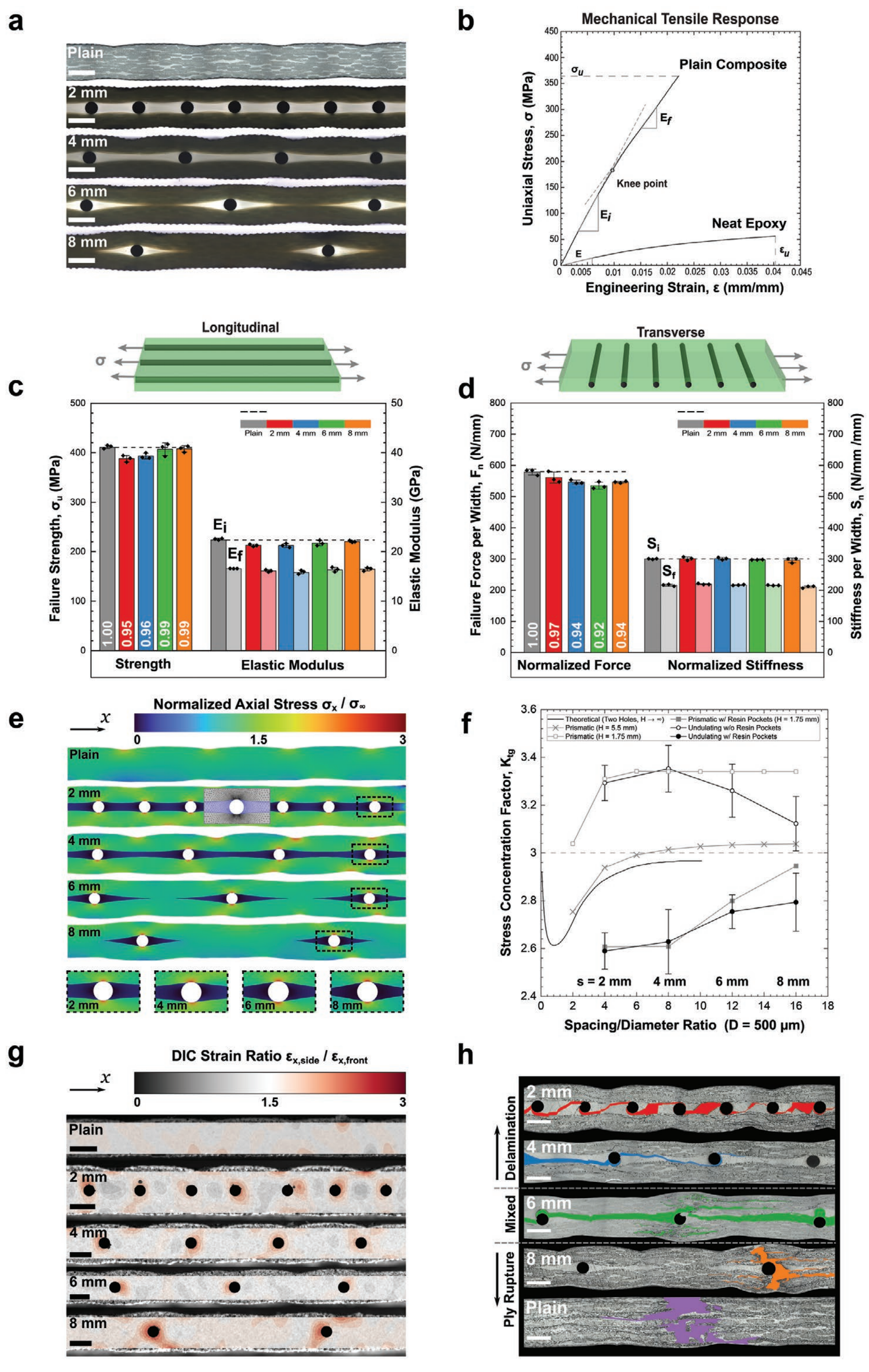

Figure 3. Structural integrity evaluation. a) Optical micrographs of transversely oriented channel cross-sections with varying spacing (s = 2, 4, 6, and 8 mm) and also a non-vascular, plain composite (scale bar = 1 mm). b) Constituent material tensile response for plain composite and epoxy matrix. c) Failure strength and elastic moduli summary for longitudinal channel geometries (dashed lines signify plain composite average and numbers at the bottom of bar plots represent the normalized values to the plain, non-vascular control. d) Failure force per unit width and stiffness per unit width (initial and final) summary for transversely oriented channels. e) Normalized axial stress contours from linear elastic finite element analysis (FEA) of transverse geometries. Representative mesh shown for 2 mm contour depicts element size refinement in vicinity of maximum stress. f) Comparison of gross stress concentration factor (K_{tg}) from FEA simulations versus theoretical behavior for an infinite width plate containing two holes. g) Normalized axial strain contours from digital image correlation (DIC). h) Post-mortem micrographs of failed samples depicting transition of failure mode based on vascular spacing. (Note: error bars in (c) and (d) represent the standard deviation from three samples tested; error bars in (f) represent the standard deviation from the respective number of channels for each spacing configuration shown in (e)).

plain composite exhibits a bilinear response as a result of matrix cracking between fiber tows transverse to the loading direction.[100] The change in composite modulus occurs around 1% strain (i.e., the knee point), where the initial (E_i) and final (E_f) moduli are determined from a linear regression based on least-squares. We also determined Poisson's ratio for both materials in the initial linear elastic regime using DIC data via the ratio of lateral to axial strains (Section S3, Supporting Information).

Figure 3c provides a summary of tensile properties (i.e., failure strength and moduli) for the longitudinal samples across all channel spacings (s = 2, 4, 6, and 8 mm) in comparison to the plain composite. Despite the presence of surface/thickness undulations, the longitudinally-oriented samples have nearly prismatic cross-sections along the length. Precise area measurements from optical micrographs (including undulations and neglecting micro-channels) allowed the direct calculation of normal stress, that is, $\sigma = \frac{force}{area}$. We observed a maximum 5% ultimate strength reduction for the 2 mm spacing compared to the plain, non-vascular composite. The reduction in ultimate strength for the 4 mm spacing is 4%, and while statistically insignificant from the 2 mm spacing, both are statistically significant compared to the plain composite strength. Increased micro-channel spacing mitigates the longitudinal strength reduction, with only 1% average drop for the 6 and 8 mm samples; both of these strengths remain within the standard deviation of the plain composite strength and are thus statistically insignificant. A similar increasing trend for moduli versus channel spacing was observed, which we attribute to a decreased areal percentage of more compliant resin pockets. We calculated theoretical strength and moduli based on the rule of mixtures and found the overall contribution of epoxy resin pockets to these quantities is small (< 2%); this relatively small contribution can be attributed to the low volume percentage (< 15%) and reduced mechanical properties of the epoxy compared to the fiber-reinforced composite (Section S4, Supporting Information). Thus, in the aligned longitudinal configuration, the impact of micro-channels on structural performance is minimal compared to a plain non-vascular woven composite laminate.

The second case we studied—vasculature oriented transverse to the loading direction—is far more interesting. Here due to the thickness undulations, it is not valid to calculate engineering stress using the ratio of force over area as the cross-section varies along the length. We therefore considered force and stiffness per-unit-width to compensate for thickness undulations as well as varying sample widths, resulting from fabrication constraints. Despite these geometrical variations, each sample (coming from a single composite panel) contains the same amount of reinforcing layers, which primarily governs the mechanical response. Figure 3d summarizes the mechanical properties for plain and vascular composites tested in the transverse direction. In contrast to the trends observed from the longitudinal tests, as channel spacing increases, stiffness per width (S_n) remains largely unchanged. An average reduction (maximum of 8%) in failure force per width (F_n) occurs at 6 mm spacing that is statistically insignificant from the 8 mm results, but statistically significant from the plain composite value. Overlaps in error bars amongst vascular samples make it difficult to fully explain the observed trends and the impact on structural integrity.

To better understand the effects of micro-channels, surrounding resin domains and surface undulations, we performed a 2D linear elastic finite element analysis (FEA) in COMSOL (v.5.6)[101] on geometries closely resembling the samples (i.e., actual surface undulations but uniform, yet representative channel diameter and resin domains; see Section S5, Supporting Information). Normalized axial stress contours provided in Figure 3e show expected stress concentrations at the top/bottom of the vascules (cf. refs. [27,83,102,103]) as well as strong interactions with surface undulations, which have not been adequately studied. To decode these complex stress interactions and the effect of resin pockets on tensile integrity, we performed additional FEA simulations on a series of prismatic geometries both with and without resin domains. As shown in Figure 3f, for a prismatic, homogeneous, and isotropic medium with two micro-channels, the gross stress concentration factor (K_{tg}, see Equation (2)) increases as the height-(i.e., thickness)-to-diameter ratio decreases. Mathematically, K_{tg} is calculated as:

$$K_{tg} = \frac{\sigma_{\max}}{\sigma_{\infty}} \tag{2}$$

where σ_∞ is the (applied) far-field stress and σ_{max} is the maximum stress (for our geometries and loading conditions, $\sigma_{max} = \sigma_x$ occurs at either the top or bottom points on the surface of the microchannels).

Also, as the channel spacing-to-diameter ratio increases, the stress concentrations increase and reach a plateaued value around 3.3 for a representative thickness (H = 1.75); note for a plate with infinite thickness, the well-known asymptotic stress concentration solution is 3.0.[104] Interestingly, an important observation from this study shows the presence of resin pockets (which are more compliant, E_{epoxy} = 2.5 GPa, than the homogenized composite material, $E_{composite}$ = 20 GPa), serve to decrease the stress concentrations for all spacings with the most pronounced benefit (≈ 20% reduction) for the 2 and 4 mm spacings containing contiguous epoxy regions. When comparing FEA results for two-channel prismatic models against those containing multiple channels and surface undulations, we again observe a reduction in stress concentrations around the micro-channels due to the resin pockets. However, the undulations and their relative locations with respect to the micro-channels introduce variability in the stress concentrations. Full-field strain contours via DIC provided in Figure 3g corroborate the complex structural interaction (observed in the FEA simulations) between surface topology and internal micro-channels.

Post-mortem microscopic imaging of failed samples shown in Figure 3h provides insight into the damage behavior. Closer channel spacings of 2 and 4 mm exhibit a dominant delamination mode through the contiguous resin region, the 8 mm spaced samples predominantly failed by ply-rupture similar to the plain composites, and the 6 mm spaced samples exhibited a mixed delamination/rupture behavior. We hypothesize that damage initiates at the location of maximum stress concentration around the channels, however, fracture propagation is dictated by a myriad of material, geometrical, and microstructural factors. While beyond the scope of this study, we intend to conduct a comprehensive investigation, combining experimental and computational approaches, to unravel the effects of geometrical (e.g., undulation-channel interactions), material (e.g., nonlinear and orthotropic) properties, and microstructural features (e.g., fiber orientation) on damage initiation and propagation.

Regardless of how complex the structural behavior, incorporation of pervasive microvasculature within fiber-reinforced composites, if designed properly, can provide multi-functionality without significant detriment to mechanical properties. For example, in our experiments, we only observed a maximum of 5% reduction in tensile failure strength for longitudinally-oriented micro-channels, occurring from the 2 mm vascular spacing which resulted in the largest resin pocket volume fraction. However, for transversely-oriented micro-channels, the same 2 mm spacing resulted in the highest failure force presumably due to lower stress concentrations resulting from: i) smaller spacing to diameter/ratio (supported by theory) and ii) contiguous, compliant resin pocket region that enhances stress reduction (revealed by simulations). Although we have only investigated in-plane tension, we expect compression to have a more pronounced effect given the ply waviness amplified by sacrificial elements; such geometrical imperfections are known to reduce local buckling strength of load bearing fibers.[27,83]

Aside from structural damage, deterioration from thermal loads is also a concern for epoxy-matrix composites, specifically as the thermoset matrix transforms from a glassy to a rubbery state near the glass transition temperature.[12] However, multi-functional microvasculature can be further leveraged to provide an additional ability for combating thermal degradation via circulation of liquids[13] or gaseous coolants.[44]

5. Thermal Regulation

Vascular-enabled, actively-cooled composites can provide lightweight structural performance and removal of excess heat in thermally demanding applications, particularly those in which FRP materials have been traditionally excluded due to lower thermal stability of the polymer matrix compared to metallic or ceramic counterparts. Some modern applications we envision for active-cooling in composites include high-power antennas[105,106] and laser diode arrays,[107] hypersonic aircraft,[108,109] protective casings for fuel cells,[110,111] and electric vehicle battery packaging.[112,113]

To demonstrate the ability of our serpentine vasculature for regulating temperature and better understand governing physics, we began with a series of experiments via active pumping of liquid coolant (i.e., distilled water) under a constant heat flux. **Figure 4**a shows the experimental setup where a resistive heater substrate is used to maintain a constant heat flux of $250\,\mathrm{W m^{-2}}$ while a copper plate bonded via thermal grease between the heater and vascular composite ensures uniform heat transfer. The balsa wood platform and chloroprene foam insulation along the sides minimize heat loss to the surroundings. An infrared (IR) camera is used to acquire temperature data from the top surface of the microvascular heat exchanger along with thermocouples placed at other key measurement locations (see Experimental Section). We actively delivered the H_2O coolant using a peristaltic pump connected to tubing with a micro-nozzle that was inserted into the inlet channel, with the water exiting the composite through an outlet using the same tubing/nozzle configuration. An important metric for microfluidics is the pressure drop (ΔP) across a length (L) of channel, where the resulting flowrate (Q) for a given input pressure scales inversely proportional to the 4th power of the (circular) channel diameter (D) according to the Hagen–Poiseuille relation: $\Delta P = Q\frac{128\mu L}{\pi D^4}$, where μ is the dynamic viscosity of the fluid.[84] Typically, a faster coolant flow rate increases heat extraction, but naturally results in a higher pressure drop. Herein we wanted to compare the cooling efficiency of our various serpentine patterns (s = 2, 4, 6, and 8 mm) under a constant pumping power. Due to the increased channel lengths and the presence of a larger number of turns for tighter spacings, the pressure drop for each serpentine configuration varied. In order to achieve constant pumping power, we determined the flowrates for each single-channel spacing corresponding to an input pressure of 300 kPa (see Section S6, Supporting Information). The respective flowrates (7.0, 12.5, 17.7, and 22.3 mL min^{-1}) were then achieved using the peristaltic pump through a calibration procedure, where no more than ± 4% variation occurred from the pressure-driven measurements. For the dual-channel configuration (Figure 2b), the measured flow rates in the top and bottom microvascular networks exhibited no statistical difference. This further confirmed consistency in our microvascular fabrication process based on 3D printing of sacrificial polymer and subsequent vaporization.

We began the active-cooling experiments by simultaneously heating and cooling the composites until a cold steady state (CSS) condition was reached (Figure 4b). This CSS condition was determined when the average top surface temperature of the composite, measured by the IR camera, varied less than ± 0.2 °C (i.e., the camera precision) over a 10 min period. Figure 4b shows a representative top surface temperature distribution at the CSS condition (dashed lines) along with the average IR camera temperature and thermocouple measurements over time.

A purely experimental study on our serpentine composites cannot capture the effect without resin pockets, which are fabrication-induced domains that have lower thermal conductivity than the surrounding composite (Section S7, Supporting Information), and could impact the overall active-cooling performance. Similar to the structural integrity investigation, we leveraged computational modeling to quantify the effects of these micro-scale features on heat transfer characteristics. To this end, we created 3D models of our vascular composites both with and without resin pockets, and carried out numerical simulations by solving the energy-momentum coupled equations using the finite volume method (FVM) in ANSYS FLUENT (v.18.2)[114] (Section S8, Supporting Information).

Figure 4c shows the top surface temperature distributions obtained from the experiments at the CSS condition and corresponding steady-state simulations for single-channel composites across all channel spacings. Without active-cooling, a steady-state temperature of 35 °C is reached (Section S9, Supporting Information), whereas the fastest flow-rate (22.3 mL min^{-1}) occurring for the 8 mm spacing, reduces the maximum temperature to 22.1 °C. While the experimental temperature contours do not exactly match the simulation results, they show good agreement in capturing the enhanced

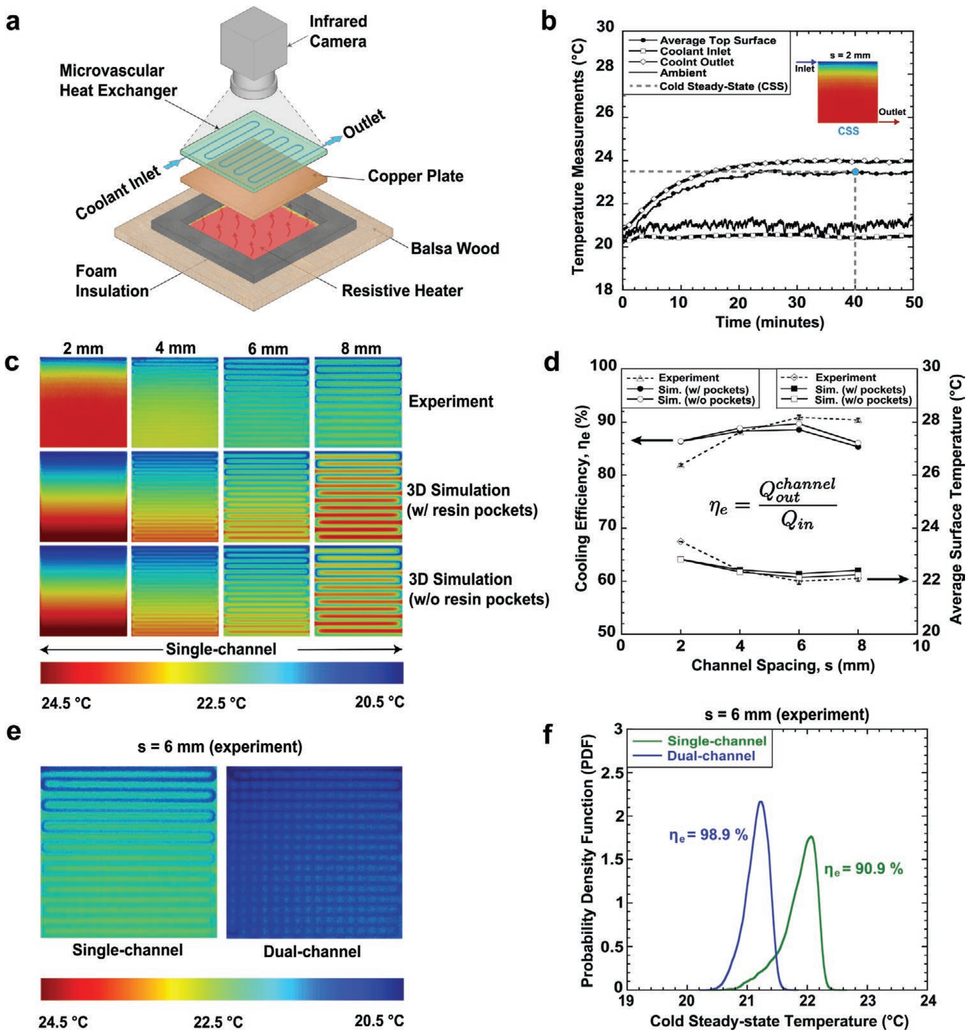

Figure 4. Active-cooling performance. a) Schematic of experimental setup showing resistive heater substrate and overhead mounted infrared (IR) camera used for thermal imaging throughout the experiment. b) Typical temperature measurements recorded by IR camera (average top surface) and various thermocouples (ambient, coolant inlet/outlet) over time along with corresponding cold steady-state (CSS) surface temperature distribution. c) Top surface temperature contour plots at CSS obtained from experiment and 3D ANSYS FLUENT simulation (with and without modeling resin pocket geometry) for single-channel composites of varying channel spacing ($s = 2$, 4, 6, and 8 mm). d) Cooling efficiency (η_e: ratio of heat extracted by channel to heat supplied by heater, Equation (3)) and average surface temperature obtained from both experiments and simulations for single-channel composites. e) Top surface temperature contours at CSS from experiments for single- and dual-channel composites with a fixed 6 mm serpentine spacing. f) Calculated cooling efficiencies and probability density functions (PDF) constructed from top surface temperature measurements at CSS for single- and dual-channel composites with 6 mm channel spacing. (Note: error bars in (d) represent the standard deviation from three experiments conducted on the same sample for each spacing configuration).

cooling performance for larger compared to smaller spacings on account of increased flow-rates resulting from lower pressure-drops for shorter channel lengths. The experimental temperature contours for the smaller channel spacings (i.e., 2 and 4 mm) are warmer than corresponding simulations, whereas, the larger channel spacings (i.e., 6 and 8 mm) show cooler experimental results compared to simulations. A plausible reason for the slight discrepancies in surface temperatures is the adiabatic boundary conditions assumed in the simulations; such idealized conditions are not completely enforced by the foam insulation in the experiments (Section S9, Supporting Information). Close agreement between surface temperature distributions from FLUENT simulations with and without resin pockets indicate these localized epoxy domains do not have a significant effect on active-cooling. To further investigate the effect of the structural host thermal conductivity on heat transfer performance, we performed a series of 2D simulations based on the interface enriched generalized finite element formulation (IGFEM)[115,116] (Section S10, Supporting Information) comparing both glass- and carbon-fiber composites with aluminum (Section S11, Supporting Information). Despite the 100-fold increase in thermal conductivity for an aluminum panel compared to our glass-fiber composite, a less than 1 °C change in average surface temperature occurred for the prescribed flow rates and assumed equivalent heat transfer coefficient across the different materials. This further confirms the relatively minor role of the host material's thermal conductivity observed in our steady-state simulations under the given flow rates.

To quantify the overall active-cooling performance of our microvascular composites, we considered a cooling efficiency metric (η_e, Equation (3)),[117] defined as the ratio of heat extracted by the fluid in the serpentine micro-channel ($Q_{out}^{channel}$) to the total heat supplied to the composite (Q_{in}):

$$\eta_e = \frac{Q_{out}^{channel}}{Q_{in}} \tag{3}$$

The heat extracted by the liquid flowing in the channel was determined from an energy balance equation at the cold steady-state (Section S12, Supporting Information).

Figure 4d compares the calculated cooling efficiencies and average top surface temperature distributions for single-channel composites obtained via experiments and 3D FLUENT simulations both with and without resin pockets. Up to 6 mm channel spacing, as flow rates increase due to a reduction in pressure drop, improved active cooling performance as well as lower average top surface temperatures are produced by the experiments and simulations. However for the 8 mm spacing, the experiments show a plateau in cooling efficiency while simulations show a slight (< 5%) decrease compared to the 6 mm spacing. We attribute this diminishing cooling behavior to a competing effect between lower serpentine channel density and higher flow rate for a shorter, less tortuous micro-channel on account of the constant pumping power input condition. Prescribing the flow rate from the 8 mm spacing (i.e., 22.3 mL min^{-1}) for a 6 mm spacing shows a continued increase in computed cooling efficiency (Section S13, Supporting Information), reinforcing our hypothesis.

We also compared the 6 mm spaced single-channel composite to a dual-channel configuration of identical spacing and subject to the same constant pumping power input condition; note since pressure is identical after a bifurcation, the prescribed flow rate for each channel in the dual configuration is equal to the single-channel at 17.7 mL min^{-1}. Figure 4e contains the top surface temperature distributions for the 6 mm single- and dual-channel actively-cooled composites, where the dual configuration exhibits a lower overall surface temperature and greater uniformity. To quantify this cooling enhancement, we utilized a probability density function (PDF)[117] as plotted in Figure 4f for each case. Here we considered the most probable temperature (MPT) or peak of the PDF distribution in the domain and also range (R) of temperatures as measures of uniformity, where a lower peak value and narrower range indicate better cooling. While the single-channel (MPT/R: 22.2/2.2 °C) attains 91% efficiency, the dual-channel composite (MPT/R: 21.3/1.5 °C) achieves 99% cooling efficiency on account of better vascular distribution and greater fluid exchange for a given input pressure.

Curious to know whether the electrically (and thermally) conductive liquid metal (i.e., EGaIn) employed for EM modulation would outperform the distilled water coolant, we performed a non-dimensional analysis followed by a computational investigation (w/o resin pockets) using FLUENT and IGFEM (Section S14, Supporting Information). The simulation results in Figures S17 and S18, Supporting Information, are consistent with our analytical observation that the Péclet number,[118] a ratio of advective to conductive heat transfer (also product of Reynolds and Prandtl numbers), governs the cooling efficiency. Thus, for a given channel diameter and prescribed volumetric flowrate, heat transfer is proportional to the product of coolant density (ρ) and specific heat capacity (c_p) divided by thermal conductivity (k) of the fluid (i.e., $\frac{\rho c_p}{k}$). Contrary to intuition, even though thermal conductivity of the EGaIn is orders of magnitude higher than water, the interplay between specific heat and density make distilled water a better coolant for our microvascular composite heat exchanger at steady-state. However, highly transient applications or those involving significant heat fluxes and temperatures exceeding the boiling point of water can benefit from a liquid-metal coolant or other thermal fluid with a higher temperature window.

Our investigation into the heat transfer characteristics of microvascular composites reveals that the pervasive serpentine channel topology and coolant properties (for a fixed combined heat transfer coefficient, Section S11, Supporting Information) play a more critical role than thermal conductivity of the host material on active-cooling performance. For a prescribed pumping power, a larger spacing and thus shorter, less tortuous micro-channel has a lower pressure drop resulting in faster flow-rates and enhanced active-cooling (i.e., lower average surface temperature and greater heat extraction by the fluid) up to a point. As channels are spaced further apart, despite faster flow rates, cooling efficiency will eventually plateau/decrease. For a given spacing, increased flow rates will continue to improve cooling performance, but at a reduced rate. Increasing the thermal conductivity of the host material results in marginal improvement in cooling efficiency, and as such, localized resin pockets with lower conductivity do not significantly impact overall heat transfer. The thermal properties of the fluid play a more critical role in heat exchange, which is proportional to the Péclet number. Thus, increasing the density and specific heat of the liquid coolant will enhance heat extraction from the system for a given volumetric flow rate and channel dimension. The orthogonal, dual-layer vascular configuration introduced here is a viable route to enhance both cooling efficiency and temperature uniformity.

Owing to the reconfigurable nature of our proposed structural metamaterial, it is possible to obtain on-the-fly configurations across multiple physics. For example, a dual-layer configuration could be deployed such that one layer filled with an electrically/thermally conductive fluid provides both polarization-selective EM filtering and active-cooling, while another layer containing a circulated dielectric coolant enhances thermal protection without affecting EM shielding. Future in-depth studies are required to fully understand such complex and coupled problems, and here we have laid the foundation for further explorations.

6. Conclusion

This comprehensive experimental/numerical investigation has shown that multi-physical properties, including electromagnetic reflectivity and thermal regulation, can be dynamically modulated within a structural fiber-composite via substitution of the fluid sequestered within a simple serpentine vasculature. We revealed that both the pervasive micro-channel topology and resulting composite micro-structure are integral to the performance of such multifunctional microvascular metamaterials. Denser vasculature provides enhanced RF wave filtering; however, closely spaced vasculature is not necessarily best for active-cooling due to increased flow resistance. Also, despite widespread vascularization, augmented material micro-architecture (i.e., resin pockets) does not adversely affect mechanical (tensile) properties and preserves multi-functionality. Given the vitality of fiber-reinforced polymer composites to modern structures (e.g., spacecraft, electric vehicles, corrosion-resistant infrastructure, wind turbine blades), embracing such multifunctional materials will be critically important for expanding operational envelopes.

However, to fully leverage multi-physics performance in envisioned microvascular materials, further explorations are needed to better understand individual physics as well as competing factors across scientific domains. Several spin-off questions that a warrant comprehensive investigation are: How does material heterogeneity/anisotropy affect damage and fracture propagation under a general state of stress? How does localized damage influence electromagnetic reconfiguration? What role do thermal gradients from active-cooling play on stress concentrations? From a material design perspective, as computational tools evolve (e.g., topology optimization[119,120]), what types of objective functions are valid for such cross-cutting materials, and how might one incorporate biological principles[121–123] into the design/manufacturing process? Noting a recent work on optimal material distribution for flow problems,[124] the rate of dissipation—a physical quantity with universal applicability from its firm thermodynamic underpinning—seems to be a suitable candidate for an objective function. Finally, future research endeavors addressing these and other fundamental questions will create a body of scientific knowledge enabling real-world translation and creation of new functionalities within multifunctional microvascular metamaterials.

Supporting Information

Supporting Information is available from the Wiley Online Library or from the author.

Acknowledgements

This work has been financially supported by the Air Force Office of Scientific Research (grant number FA9550-18-1-0048). The authors extend their gratitude to Alexander Snyder for insightful research discussions on heat transfer, Prof. Mark Pankow and Brandon Hearley for DIC-related equipment and expertise, Sarah Mann for assistance with graphics, Tejasree Phatak for thermal conductivity measurements, and Dr. Chris Mangun at CU Aerospace for providing sacrifical PLA filament.

Conflict of Interest

The authors declare no conflict of interest.

Author Contributions

J.F.P. directed the research and together with K.R.S. conceived the serpentine microvascular design. U.D. and Z.J.P. fabricated the vascular composites. K.R.S. performed the electromagnetic experiments and analyses. U.D. performed the thermal experiments/analyses while R.P. and A.R.N. performed the thermal simulations. Z.J.P. and U.D. performed the structural experiments/analyses while K.B.N., P.Z., and S.S. performed the structural simulations. K.B.N. provided theoretical and numerical insights into the thermal and structural problems. All authors participated in discussions of the research and wrote the manuscript.

Data Availability Statement

Research data are not shared.

Keywords

bioinspired, electromagnetic modulation, fiber-composites, metamaterial, microvascular, multifunctional, thermal regulation

Received: April 13, 2021
Revised: June 22, 2021
Published online:

[1] J. B. Reece, L. A. Urry, M. L. Cain, S. A. Wasserman, P. V. Minorsky, R. B. Jackson, *Campbell Biology*, 12th ed., Pearson, Boston **2020**.
[2] V. S. Kopylova, S. E. Boronovskiy, Y. R. Nartsissov, *Biochem. Soc. Trans.* **2017**, *45*, 839.
[3] A. Guyton, J. Hall, *Textbook of Medical Physiology*, 11th ed., Saunders Elsevier, Philadelphia **2005**.
[4] R. Trask, I. Bond, *Smart Mater. Struct.* **2006**, *15*, 704.
[5] K. S. Toohey, N. R. Sottos, J. A. Lewis, J. S. Moore, S. R. White, *Nat. Mater.* **2007**, *6*, 581.
[6] B. J. Blaiszik, S. L. Kramer, S. C. Olugebefola, J. S. Moore, N. R. Sottos, S. R. White, *Annu. Rev. Mater. Res.* **2010**, *40*, 179.
[7] C. E. Diesendruck, N. R. Sottos, J. S. Moore, S. R. White, *Angew. Chem., Int. Ed.* **2015**, *54*, 10428.
[8] J. F. Patrick, M. J. Robb, N. R. Sottos, J. S. Moore, S. R. White, *Nature* **2016**, *540*, 363.
[9] A. Cohades, C. Branfoot, S. Rae, I. Bond, V. Michaud, *Adv. Mater. Interfaces* **2018**, *5*, 1800177.
[10] B. D. Kozola, L. A. Shipton, V. K. Natrajan, K. T. Christensen, S. R. White, *J. Intell. Mater. Syst. Struct.* **2010**, *21*, 1147.
[11] D. M. Phillips, M. R. Pierce, J. W. Baur, *Composites, Part A* **2011**, *42*, 1609.
[12] A. M. Coppola, A. S. Griffin, N. R. Sottos, S. R. White, *Composites, Part A* **2015**, *78*, 412.
[13] A. M. Coppola, L. G. Warpinski, S. P. Murray, N. R. Sottos, S. R. White, *Composites, Part A* **2016**, *82*, 170.
[14] S. J. Pety, M. H. Y. Tan, A. R. Najafi, P. R. Barnett, P. H. Geubelle, S. R. White, *Int. J. Heat Mass Transfer* **2017**, *115*, 513.
[15] A. J. King, J. F. Patrick, N. R. Sottos, S. R. White, G. H. Huff, J. T. Bernhard, *IEEE Antennas Wireless Propag. Lett.* **2013**, *12*, 828.
[16] D. Hartl, G. Frank, G. Huff, J. Baur, *Smart Mater. Struct.* **2016**, *26*, 025001.
[17] G. H. Huff, H. Pan, D. J. Hartl, G. J. Frank, R. L. Bradford, J. W. Baur, *IEEE Trans. Antennas Propag.* **2017**, *65*, 2282.
[18] L. Song, W. Gao, C. O. Chui, Y. Rahmat-Samii, *IEEE Trans. Antennas Propag.* **2019**, *67*, 2886.
[19] A. S. Griffin, H. Pan, J. D. Barrera, G. H. Huff, S. R. White, N. R. Sottos, *Smart Mater. Struct.* **2020**, *29*, 045032.
[20] J. W. Pang, I. P. Bond, *Compos. Sci. Technol.* **2005**, *65*, 1791.

[21] A. Kousourakis, A. Mouritz, M. Bannister, *Compos. Struct.* **2006**, *75*, 610.
[22] O. Rifaie-Graham, E. A. Apebende, L. K. Bast, N. Bruns, *Adv. Mater.* **2018**, *30*, 1705483.
[23] C. Luan, X. Yao, C. Zhang, J. Fu, B. Wang, *Compos. Sci. Technol.* **2020**, *188*, 107986.
[24] G. Williams, R. Trask, I. Bond, *Composites, Part A* **2007**, *38*, 1525.
[25] M. Motuku, U. Vaidya, G. Janowski, *Smart Mater. Struct.* **1999**, *8*, 623.
[26] S. Bleay, C. Loader, V. Hawyes, L. Humberstone, P. Curtis, *Composites, Part A* **2001**, *32*, 1767.
[27] C.-Y. Huang, R. Trask, I. Bond, *J. R. Soc., Interface* **2010**, *7*, 1229.
[28] C. Norris, I. Bond, R. Trask, *Composites, Part A* **2011**, *42*, 639.
[29] C. Norris, I. Bond, R. Trask, *Compos. Sci. Technol.* **2011**, *71*, 847.
[30] J.-C. Hung, D.-H. Chang, Y. Chuang, *J. Power Sources* **2012**, *198*, 158.
[31] M. Lima, J. Sakamoto, J. Simoes, R. Riva, *Phys. Procedia* **2013**, *41*, 572.
[32] T. Dixit, I. Ghosh, *Renewable Sustainable Energy Rev.* **2015**, *41*, 1298.
[33] J.-H. Huang, J. Kim, N. Agrawal, A. P. Sudarsan, J. E. Maxim, A. Jayaraman, V. M. Ugaz, *Adv. Mater.* **2009**, *21*, 3567.
[34] D. Therriault, S. R. White, J. A. Lewis, *Nat. Mater.* **2003**, *2*, 265.
[35] J. A. Lewis, *Adv. Funct. Mater.* **2006**, *16*, 2193.
[36] D. Therriault, R. F. Shepherd, S. R. White, J. A. Lewis, *Adv. Mater.* **2005**, *17*, 395.
[37] M.-U. Saeed, Z. Chen, B. Li, *Composites, Part A* **2015**, *78*, 327.
[38] I. P. S. Qamar, N. R. Sottos, R. S. Trask, *Multifunct. Mater.* **2020**, *3*, 013001.
[39] A. P. Esser-Kahn, P. R. Thakre, H. Dong, J. F. Patrick, V. K. Vlasko-Vlasov, N. R. Sottos, J. S. Moore, S. R. White, *Adv. Mater.* **2011**, *23*, 3654.
[40] J. F. Patrick, B. P. Krull, M. Garg, C. L. Mangun, J. S. Moore, N. R. Sottos, S. R. White, *Composites, Part A* **2017**, *100*, 361.
[41] R. C. Gergely, S. J. Pety, B. P. Krull, J. F. Patrick, T. Q. Doan, A. M. Coppola, P. R. Thakre, N. R. Sottos, J. S. Moore, S. R. White, *Adv. Funct. Mater.* **2015**, *25*, 1043.
[42] M. Wang, C. Trlica, M. Khan, M. Dickey, J. Adams, *J. Appl. Phys.* **2015**, *117*, 194901.
[43] M. D. Dickey, *Adv. Mater.* **2017**, *29*, 1606425.
[44] M. W. McElroy, A. Lawrie, I. P. Bond, *Int. J. Heat Mass Transfer* **2015**, *88*, 284.
[45] S. J. Pety, P. X. Chia, S. M. Carrington, S. R. White, *Smart Mater. Struct.* **2017**, *26*, 105004.
[46] J. F. Patrick, K. R. Hart, B. P. Krull, C. E. Diesendruck, J. S. Moore, S. R. White, N. R. Sottos, *Adv. Mater.* **2014**, *26*, 4302.
[47] B. P. Krull, R. C. R. Gergely, W. A. Santa Cruz, Y. I. Fedonina, J. F. Patrick, S. R. White, N. R. Sottos, *Adv. Funct. Mater.* **2016**, *26*, 4561.
[48] D. Zrnic, D. Swatik, *J. Less-Common Met.* **1969**, *18*, 67.
[49] T. J. Cui, D. R. Smith, R. Liu, *Metamaterials*, Springer, New York **2010**.
[50] N. I. Zheludev, Y. S. Kivshar, *Nat. Mater.* **2012**, *11*, 917.
[51] N. Engheta, R. W. Ziolkowski, *Metamaterials: Physics and Engineering Explorations*, John Wiley & Sons, Hoboken, NJ **2006**.
[52] P. A. Deymier, *Acoustic Metamaterials and Phononic Crystals*, Vol. 173, Springer Science & Business Media, New York **2013**.
[53] B. E. A. Saleh, M. C. Teich, *Fundamentals of Photonics*, John Wiley & Sons, Hoboken, NJ **2019**.
[54] I. Staude, J. Schilling, *Nat. Photonics* **2017**, *11*, 274.
[55] R. Süsstrunk, S. D. Huber, *Science* **2015**, *349*, 47.
[56] S. D. Huber, *Nat. Phys.* **2016**, *12*, 621.
[57] T. J. Cui, M. Q. Qi, X. Wan, J. Zhao, Q. Cheng, *Light: Sci. Appl.* **2014**, *3*, e218.
[58] O. R. Bilal, A. Foehr, C. Daraio, *Adv. Mater.* **2017**, *29*, 1700628.
[59] R. Lakes, *Science* **1987**, *235*, 1038.
[60] K. Bertoldi, P. M. Reis, S. Willshaw, T. Mullin, *Adv. Mater.* **2010**, *22*, 361.
[61] S. Babaee, J. Shim, J. C. Weaver, E. R. Chen, N. Patel, K. Bertoldi, *Adv. Mater.* **2013**, *25*, 5044.
[62] H. Yang, L. Ma, *Mater. Des.* **2018**, *152*, 181.
[63] S. Yuan, C. K. Chua, K. Zhou, *Adv. Mater. Technol.* **2019**, *4*, 1800419.
[64] D. R. Smith, J. B. Pendry, M. C. Wiltshire, *Science* **2004**, *305*, 788.
[65] W. Cai, U. K. Chettiar, A. V. Kildishev, V. M. Shalaev, *Nat. Photonics* **2007**, *1*, 224.
[66] D. Schurig, J. Mock, D. Smith, *Appl. Phys. Lett.* **2006**, *88*, 041109.
[67] D. Schurig, J. J. Mock, B. Justice, S. A. Cummer, J. B. Pendry, A. F. Starr, D. R. Smith, *Science* **2006**, *314*, 977.
[68] E. B. Herbold, J. Kim, V. F. Nesterenko, S. Y. Wang, C. Daraio, *Acta Mech.* **2009**, *205*, 85.
[69] P. Wang, J. Shim, K. Bertoldi, *Phys. Rev. B* **2013**, *88*, 014304.
[70] W. Witarto, K. B. Nakshatrala, Y.-L. Mo, *Mechanics of Materials* **2019**, *134*, 38.
[71] S. H. Mousavi, A. B. Khanikaev, Z. Wang, *Nat. Commun.* **2015**, *6*, 1.
[72] S. Krödel, N. Thomé, C. Daraio, *Extreme Mech. Lett.* **2015**, *4*, 111.
[73] A. Palermo, S. Krödel, A. Marzani, C. Daraio, *Sci. Rep.* **2016**, *6*, 39356.
[74] H. W. Huang, B. Zhang, J. Wang, F.-Y. Menq, K. B. Nakshatrala, Y. Mo, K. Stokoe, *Soil Dyn. Earthquake Eng.* **2021**, *144*, 106602.
[75] M. Imran, L. Zhang, A. K. Gain, *Sci. Rep.* **2020**, *10*, 11763.
[76] E. M. Dede, F. Zhou, P. Schmalenberg, T. Nomura, *J. Electron. Packag.* **2018**, *140*, 010904.
[77] K. Bertoldi, V. Vitelli, J. Christensen, M. Van Hecke, *Nat. Rev. Mater.* **2017**, *2*, 17066.
[78] X. Xin, L. Liu, Y. Liu, J. Leng, *Adv. Funct. Mater.* **2020**, *30*, 2004226.
[79] R. H. Liu, M. A. Stremler, K. V. Sharp, M. G. Olsen, J. G. Santiago, R. J. Adrian, H. Aref, D. J. Beebe, *J. Microelectromech. Syst.* **2000**, *9*, 190.
[80] J. Park, X. Li, *J. Power Sources* **2007**, *163*, 853.
[81] C. M. Karale, S. S. Bhagwat, V. V. Ranade, *AIChE J.* **2013**, *59*, 1814.
[82] J. Zilz, C. Schäfer, C. Wagner, R. J. Poole, M. A. Alves, A. Lindner, *Lab Chip* **2014**, *14*, 351.
[83] A. Kousourakis, M. Bannister, A. Mouritz, *Composites, Part A* **2008**, *39*, 1394.
[84] B. R. Munson, T. H. Okiishi, W. W. Huebsch, A. P. Rothmayer, *Fundamentals of Fluid Mechanics*, , 7th ed., John Wiley & Sons, Hoboken, NJ **2012**.
[85] ASTM International, *ASTM D3039: Standard Test Method for Tensile Properties of Polymer Matrix Composite Materials* **2017**.
[86] H. Jeong, D. H. Le, D. Lim, R. Phon, S. Lim, *Adv. Opt. Mater.* **2020**, *8*, 1902182.
[87] A. Biswas, C. L. Zekios, S. V. Georgakopoulos, *Sci. Rep.* **2020**, *10*, 13884.
[88] J.-H. So, J. Thelen, A. Qusba, G. J. Hayes, G. Lazzi, M. D. Dickey, *Adv. Funct. Mater.* **2009**, *19*, 3632.
[89] H. K. Kim, D. Lee, S. Lim, *Sci. Rep.* **2016**, *6*, 31823.
[90] D. Lim, S. Lim, *IEEE Access* **2018**, *6*, 40854.
[91] M. D. Dickey, R. C. Chiechi, R. J. Larsen, E. A. Weiss, D. A. Weitz, G. M. Whitesides, *Adv. Funct. Mater.* **2008**, *18*, 1097.
[92] M. I. Kontorovich, V. Y. Petrun'kin, N. A. Yesepinka, M. I. Astrakhan, *Radio Eng Electron. Phys.* **1962**, *7*, 222.
[93] L. C. Shen, *Applied Electromagnetism*, Brooks/Cole, Pacific Grove **1987**.
[94] J. Ma, V. T. Bharambe, K. A. Persson, A. L. Bachmann, I. D. Joshipura, J. Kim, K. H. Oh, J. F. Patrick, J. J. Adams, M. D. Dickey, *ACS Appl. Mater. Interfaces* **2021**, *13*, 12709.
[95] A. T. Nguyen, A. C. Orifici, *Composites, Part A* **2012**, *43*, 1886.
[96] K. Shivakumar, A. Bhargava, *J. Compos. Mater.* **2005**, *39*, 777.
[97] H. Ghayoor, C. C. Marsden, S. V. Hoa, A. R. Melro, *Composites, Part A* **2019**, *117*, 125.

[98] M. A. Sutton, W. Wolters, W. Peters, W. Ranson, S. McNeill, *Image Vision Comput.* **1983**, *1*, 133.
[99] L. Lamberti, M.-T. Lin, C. Furlong, C. Sciammarella, P. L. Reu, M. A. Sutton, *Advancement of Optical Methods and Digital Image Correlation in Experimental Mechanics*, Vol. 3, Springer, Berlin **2019**.
[100] T. Osada, A. Nakai, H. Hamada, *Compos. Struct.* **2003**, *61*, 333.
[101] COMSOL,*COMSOL v.5.6 - Multiphysics Software* COMSOL | **2020**, https://www.comsol.com/ (accessed: May 2020).
[102] D. J. Hartl, G. J. Frank, J. W. Baur, *Compos. Struct.* **2016**, *143*, 242.
[103] W. Pilkey, D. Pilkey, Z. Bi, *Peterson's Stress Concentration Factors*, Wiley, Hoboken, NJ **2020**.
[104] C.-B. Ling, *J. Appl. Phys.* **1948**, *19*, 77.
[105] W. A. Imbriale, S. S. Gao, L. Boccia, *Space Antenna Handbook*, John Wiley & Sons, Hoboken, NJ **2012**.
[106] R. E. Hodges, N. Chahat, D. J. Hoppe, J. D. Vacchione, *IEEE Antennas Propag. Mag.* **2017**, *59*, 39.
[107] X.-D. Zhang, X.-P. Li, Y.-X. Zhou, J. Yang, J. Liu, *Appl. Therm. Eng.* **2019**, *162*, 114212.
[108] B. Youn, A. Mills, *J. Thermophys. Heat Transfer* **1995**, *9*, 136.
[109] J.-J. Gou, Y. Chang, Z.-W. Yan, B. Chen, C.-L. Gong, *Appl. Therm. Eng.* **2019**, *159*, 113938.
[110] B. Ramos-Alvarado, P. Li, H. Liu, A. Hernandez-Guerrero, *Appl. Therm. Eng.* **2011**, *31*, 2494.
[111] G. Zhang, S. G. Kandlikar, *Int. J. Hydrogen Energy* **2012**, *37*, 2412.
[112] S. Wang, Y. Li, Y.-Z. Li, Y. Mao, Y. Zhang, W. Guo, M. Zhong, *Appl. Therm. Eng.* **2017**, *123*, 929.
[113] W. Wu, S. Wang, W. Wu, K. Chen, S. Hong, Y. Lai, *Energy Convers. Manage.* **2019**, *182*, 262.
[114] ANSYS, *ANSYS FLUENT v.18.2 - CFD Software | ANSYS* **2018**, https://www.ansys.com/ (accessed: May 2020).
[115] S. Soghrati, A. M. Aragón, C. Armando Duarte, P. H. Geubelle, *Int. J. Numer. Methods Eng.* **2012**, *89*, 991.
[116] S. Soghrati, A. R. Najafi, J. H. Lin, K. M. Hughes, S. R. White, N. R. Sottos, P. H. Geubelle, *Int. J. Heat Mass Transfer* **2013**, *65*, 153.
[117] R. Pejman, S. H. Aboubakr, W. H. Martin, U. Devi, M. H. Y. Tan, J. F. Patrick, A. R. Najafi, *Int. J. Heat Mass Transfer* **2019**, *144*, 118606.
[118] R. Chhabra, V. Shankar, *Coulson and Richardson's Chemical Engineering*, Butterworth-Heinemann, Oxford **2017**.
[119] A. R. Najafi, M. Safdari, D. A. Tortorelli, P. H. Geubelle, *Comput. Methods Appl. Mech. Eng.* **2015**, *296*, 1.
[120] J. Wu, O. Sigmund, J. P. Groen, *Struct. Multidiscip. Optim.* **2021**, *63*, 1455.
[121] P. Fratzl, R. Weinkamer, *Prog. Mater. Sci.* **2007**, *52*, 1263.
[122] J. Aizenberg, P. Fratzl, *Adv. Mater.* **2009**, *21*, 387.
[123] U. G. K. Wegst, H. Bai, E. Saiz, A. P. Tomsia, R. O. Ritchie, *Nat. Mater.* **2015**, *14*, 23.
[124] T. Phatak, K. B. Nakshatrala, *Transp. Porous Media* **2021**, *138*, 401.